J. Eur. Opt. Society-Rapid Publ. 2024, **20**, 3
© The Author(s), published by EDP Sciences, 2024
https://doi.org/10.1051/jeos/2024002
Available online at: https://jeos.edpsciences.org

Journal of the European Optical Society-Rapid Publications

EOSAM 2023
Guest editors: Patricia Segonds, Guy Millot and Bertrand Kibler

RESEARCH ARTICLE OPEN ACCESS

Bispectral optical cavity based on twin metamirrors

Liam Shelling Neto[1,2,3,*], Johannes Dickmann[1,2,3], Steffen Sauer[1,2,3,4], and Stefanie Kroker[1,3,4]

[1] Technical University of Braunschweig, Institute for Semiconductor Technology, Hans-Sommer-Str. 66, Braunschweig, Germany
[2] CAVITY technologies UG (haftungsbeschraenkt), Wilhelmsgarten 3, Braunschweig, Germany
[3] Laboratory for Emerging Nanometrology (LENA), Langer Kamp 6a/b, Braunschweig, Germany
[4] Physikalisch-Technische Bundesanstalt, Bundesallee 100, Braunschweig, Germany

Received 12 December 2023 / Accepted 18 January 2024

Abstract. In this work, we introduce a new bispectral optical cavity concept for which we design twin pairs of highly reflective, ultra-low noise metamirrors. Metasurfaces, artificial structures composed of periodic or quasi-periodic arrays of nanostructures, offer unprecedented control over light properties, paving the way for new applications in areas from high-precision optical metrology to quantum science. Custom phase and an ultra-high reflection coefficient make these metasurfaces an ideal candidate to surpass traditional multilayer mirrors as metamirrors in precision interferometry, particularly by also minimizing thermal noise. The focusing metamirrors designed in this study expect to reflect 99.95% and 99.96% of the incoming light at both, 1064 nm and 1550 nm wavelength. Their planar counterparts even reach theoretical reflectivities of 99.9999% (1064 nm) and 99.9995% (1550 nm). These specialized metamirrors enable bispectral low-noise optical cavities, which would reduce the number of cavities in optical experiments or could be used as a versatile transfer cavity for frequency locking.

Keywords: Metasurface, Metamirror, Optical Cavity, High-Precision Optical Metrology.

1 Introduction

High-precision optical metrology hinges on the unparalleled frequency stability provided by ultra-stable laser systems. This ability to provide minimal frequency fluctuations over time has enabled research of the most fundamental laws of nature, such as variations of the fine structure constant [1] and validation tests of special relativity [2], among others. In addition, the search for gravitational waves is intrinsically linked to the use of ultra-stable lasers in interferometry [3, 4]. Nevertheless, the bottleneck of these laser systems is the thermal noise emanating from the cavities' mirror coatings [5].

Metasurfaces, i.e. micro-structured surfaces, offer a low-noise alternative to traditional Bragg mirrors by leveraging photonic resonances as the driving mechanism to achieve unprecedented reflectivities [6–9]. Essentially, the right choice of period Λ and duty cycle f can limit the number of propagating Bloch modes to two. By then carefully changing the geometric parameters, the modes interfere constructively in reflection and destructively in transmission [10]. Such metamirrors not only shape the amplitude of incident light but also control its polarization and phase to focus light from a flat surface [11]. The latter attribute is crucial, as stable optical cavities necessitate at least one focusing mirror [12]. Otherwise, divergence would cause the light to eventually leave the cavity after a few round-trips. It is important to note that the mirror's focal length does not restrict the cavity's length. In fact, typical ultra-stable cavities are constructed with lengths spanning several tens of centimeters [5, 13]. Our objective is to achieve longer focal lengths, which will expand the optical mode diameter, thereby reducing thermal noise [14]. Metaatoms, which constitute the metasurface, are central to these advanced functionalities [15–19].

In our prior work [11], we demonstrated the potential of a tandem neural network for the inverse design of metaatoms. Although effective, the present work proposes an alternative design methodology by utilizing a pathfinding algorithm. Pathfinding algorithms in metaatom design offer distinct advantages over deep learning, including enhanced interpretability due to their deterministic nature, and greater computational efficiency as they require less resources and no extensive training. Their simpler algorithmic structure allows for faster solution generation and easier integration of specific design constraints, e.g. reflectivity thresholds, making them particularly suitable for applications where speed, clarity, and simplicity are critical.

* Corresponding author: liam.shelling-neto@tu-braunschweig.de

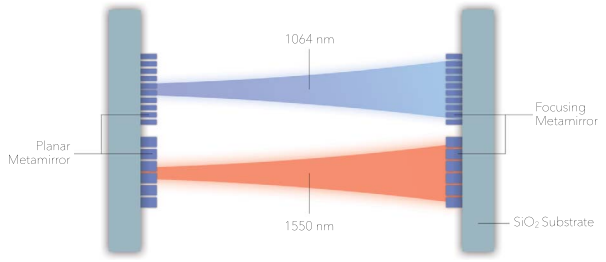

Fig. 1. Schematic of bispectral twin cavity configuration featuring two hemispherical cavities for 1064 nm and 1550 nm by utilizing dielectric metasurfaces as low-noise mirrors.

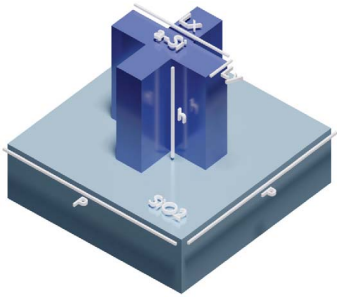

Fig. 2. Schematic of the cross-shaped metaatom with variable lateral height h, period P, and parameters L_x and L_y. The material system is chosen to be amorphous silicon (a–Si) on Fused Silica (SiO_2).

For our relatively simple metaatom designs, the utilization of pathfinding or even more rudimentary design approaches remains feasible and effective, whereas the intricacies of more complex metaatom structures necessitate the advanced capabilities of deep learning methodologies.

The main issue addressed in this work concerns the footprint of optical cavity setups. Recently, significant effort has been directed towards making optical cavities smaller and more robust [20–29]. This is aimed at reducing the footprint of experiments that require multiple optical cavities [30, 31] for enhancing their suitability for space applications [32–34] or quantum computers [35]. For instance, in the case of the latter application, a variety of laser wavelengths are crucial for qubit operations. Furthermore, the concept of a bispectral optical cavity offers the potential to transfer stability between two cavities operating at different wavelengths [31]. We begin by identifying critical parameters for each metamirror within a twin cavity configuration, as illustrated in Figure 1. Subsequently, we employ a pathfinder design strategy to create highly reflective metamirrors that focus light at the wavelengths 1064 nm and 1550 nm, suitable for bispectral optical cavities. These wavelengths are particularly suitable for bispectral optical cavities and are frequently utilized in high-precision optical metrology, such as in gravitational wave detectors [3, 36]. In the final section, we examine selected metaatoms through FEM simulations of their electric fields.

2 Setting fixed parameters

We commence by employing an amorphous Silicon (a–Si) metaatom with a cross-shape geometry with perfect periodicity atop a silicon dioxide (SiO_2) substrate, as depicted in Figure 2. The refractive indices of both materials are assumed to be $n_{\text{a-Si-1064}} = 3.536$, $n_{\text{a-Si-1550}} = 3.441$, $n_{\text{SiO2-1064}} = 1.450$, and $n_{\text{SiO2-1550}} = 1.444$ for both 1064 nm and 1550 nm, respectively. This configuration is characterized by four key parameters: L_x, L_y, h, and P. The parameters L_x and L_y are reserved for subsequent phase and amplitude modulation, while h and P are constants for both mirrors. Given that both metamirrors will share the same substrate and material composition, the structural height h is chosen to be uniform for the two target wavelengths. However, while the period P may vary between the designs of the two metamirrors, it must remain constant within each mirror to enable the integration of various metaatoms. These individual metaatoms, each producing distinct optical responses, are assembled to create the final metamirror structure.

We utilize a Python-based Rigorous Coupled Wave Analysis (RCWA) package [37] to evaluate metaatom configurations at 1064 nm and 1550 nm with regard to their phase ϕ and reflectivity R. While a global optimization algorithm could theoretically identify suitable parameters, it poses the risk of converging to highly sensitive, narrowband solutions that tend to be vulnerable to fabrication errors. Hence, a computationally manageable parametric sweep is performed of the three parameters $h \in [0.3,0.5]$ µm, $P_{1064} \in [0.45,0.6]$ µm, and $P_{1550} \in [0.75,0.95]$ µm while keeping the metaatom shape constant. These boundaries for the period are determined following equation [38]:

$$\frac{\lambda_i}{n_{\text{sub,i}} + \sin\theta_{\text{target}}} < P_i < \frac{\lambda_i}{n_{\text{sub,i}}}, \quad i \in \{1064, 1550\}, \quad (1)$$

for the wavelength λ_i, the refractive index of the substrate n_{sub}, and the propagation angle of the first diffraction order ϕ_{target}, i.e. 90°. Value ranges for the structure height are dictated by the effective wavelength inside the coating material:

$$\lambda_{\text{eff},\,i} = \frac{\lambda_i}{n_{\text{coating,i}}}, \quad i \in \{1064, 1550\}. \quad (2)$$

Here, n_{coating} refers to the refractive index of the mirror coating. These results are visualized in Figure 3 (top). To pinpoint the parameter zones achieving high reflectivity at both wavelengths, we impose a reflectivity threshold of 99.9%. Figure 3 (bottom) reveals a distinct zone meeting these criteria, from which we select $h = 395$ nm, $P_{1064} = 555$ nm, and $P_{1550} = 893$ nm.

3 Navigating the design space

We proceed to simulate combinations of L_x, $L_y \in [0.1, 0.9]$ (normalized to P) to form a design-response dataset (see Fig. 4b), wherein each pair embodies a metaatom with respective reflectivity and phase values based on L_x and L_y. To this end, we first identify a suitable flat-phase

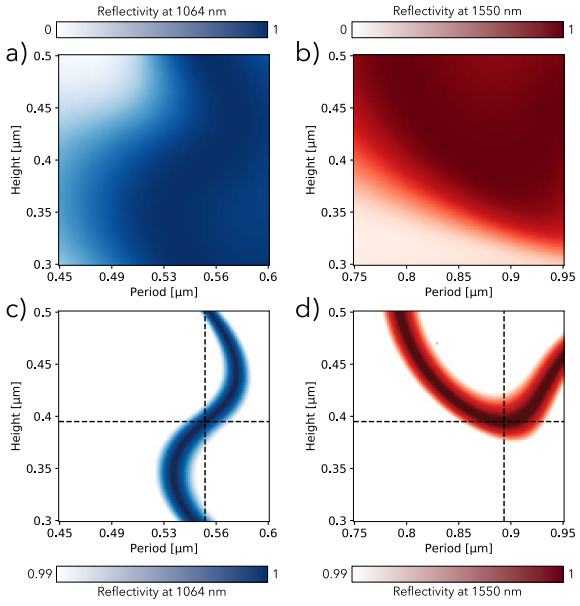

Fig. 3. RCWA simulated reflectivity for 1064 nm (left) and 1550 nm (right) of the parametric sweep of the three parameters $h \in [0.3,0.5]$ µm, $P_{1064} \in [0.45,0.6]$ µm, and $P_{1550} \in [0.75,0.95]$ µm with a fixed metaatom cross. Top. Raw Data, Bottom. Reflectivity threshold of 99.9% applied to the data.

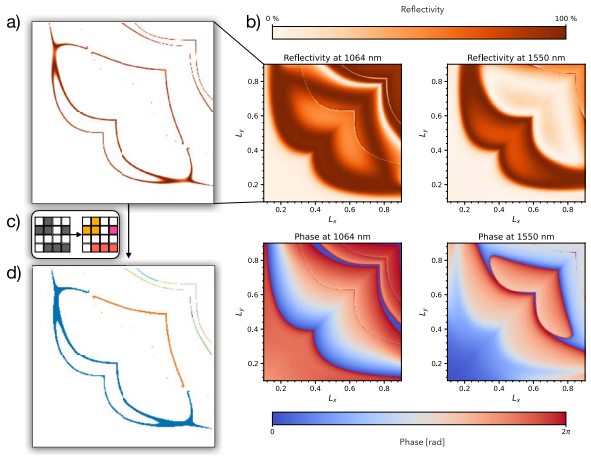

Fig. 4. a) A reflectivity threshold of 99.9% applied to the dataset. b) RCWA simulated phase and reflectivity maps for (left) 1064 nm and (right) 1550 nm. c) Scheme for labeling horizontally and diagonally connected areas. d) Color-coded high-reflectivity areas are shown for 1064 nm.

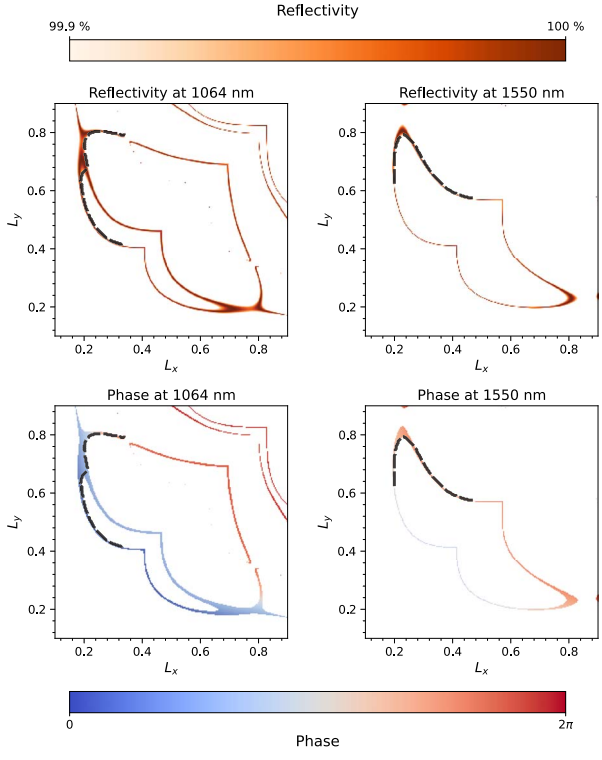

Fig. 5. Calculated phase and reflectivity maps with a threshold of 99.9% applied to the dataset. The black dotted line represents the optimal path found by the pathfinding algorithm.

metaatom by focusing solely on reflectivity values at both 1064 nm and 1550 nm, attaining theoretical reflectivities of 99.9999% for 1064 nm and 99.9995% for 1550 nm, respectively. These two metaatom species uniformly cover the two planar metamirrors for each wavelength.

While the straightforward tactic for achieving the desired phase profile would be to cherry-pick metaatoms that fit best the target phase, this could cause abrupt changes in structural parameters, thereby breaching the periodic boundary conditions assumed during simulation. In this study, we adopt a pathfinding strategy to mitigate these neighbor coupling effects [39, 40]. The pathfinding algorithm requires suitable start- and end-points, hence, we first filter the dataset with a reflectivity threshold of 99.9%, as shown in Fig. 4a), ensuring that high-reflectivity zones are retained. Utilizing Python's *scikit-image* package [41], we label diagonally connected areas (see Figs. 4c, 4d) to subsequently identify the region offering the largest phase variance.

This region aids the pathfinding algorithm in optimizing phase flexibility across the metasurface, avoiding the abrupt transitions typical of a cherry-picking approach. Figure 5 shows the optimal path found by the pathfinding algorithm that will act as the ground truth data to render the whole metamirror later on.

Additionally, we implemented a metric M to quantify relative changes in the design parameters L_x and L_y of a metaatom at position i along the radial axis of the metamirror:

$$M_i = \left| \frac{L_{x_{i+1}} - L_{x_i}}{L_{x_i}} \times 100 \right| + \left| \frac{L_{y_{i+1}} - L_{y_i}}{L_{y_i}} \times 100 \right|. \qquad (3)$$

Figure 6 validates the superiority of pathfinding over cherry-picking in minimizing M and therefore possible neighboring coupling effects. The phase gradient along the metamirror's diagonal is illustrated in Figure 7, emulating

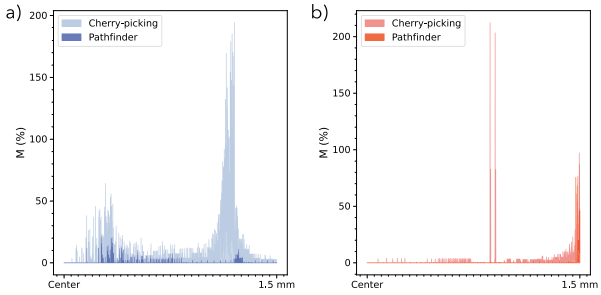

Fig. 6. Using the metric M from eq. (3) to quantify the net change in the parameters L_x and L_y for (a) 1064 nm and (b) 1550 nm.

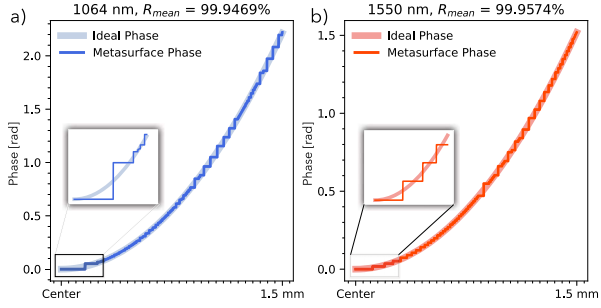

Fig. 7. Radial phase profile of the metamirror pair for a) 1064 nm and b) 1550 nm. Both mirrors yield theoretical reflectivities of $>$ 99.9% at a size of 3 $\times$ 3 mm and a focal length of 6 m. The inset shows the step-wise phase profile caused by the discrete metaatoms.

a parabolic mirror of dimensions 3 $\times$ 3 mm^2 and a focal length of 6 m. Despite small deviations from the optimum, the phase profile fits the ideal case of a conventional parabolic mirror. The inset shows the discrete nature of the metamirror caused by individual metaatoms and how the pathfinder chose different step-widths throughout the surface. This underscores the advantage of metamirrors: they enable the design of large focal lengths without the need for intricate polishing, as traditional mirrors do. It is important to note that the precise fabrication of nanostructures on curved surfaces introduces its own set of unique challenges. The designed focusing metamirrors exhibit mean reflectivities of 99.95% and 99.96% for 1064 nm and 1550 nm, respectively. That is, assuming equal illumination across the entire metamirror. In a more detailed and realistic scenario, the reflectivity of each metaatom should be considered in conjunction with the intensity of light at its specific location. For instance, with a Gaussian illumination profile featuring a beam waist of 800 µm, we observe an intensity-weighted mean reflectivity increase to 99.96% and 99.97% for wavelengths of 1064 nm and 1550 nm, respectively. These values are calculated by considering the spatial variation in illumination across the metamirror surface. Combining these focusing metamirrors with their planar counterparts allows for the calculation of the expected finesse $\mathcal{F}$, as described by [42]:

$$\mathcal{F} = \frac{\pi\sqrt{R}}{1-R} \tag{4}$$

where $R = \sqrt{R_1 * R_2}$ represents the geometric mean of the reflectivities of the individual mirrors. Applying equation (4) results in a calculated finesse of 15,526 for 1064 nm and 20,911 for 1550 nm. These values theoretically exceed the previous record measurements [9]. However, in [9], the metamirror was designed for a reflectivity of nearly 100%, yet the measurement revealed a reflectivity of only 99.95%. It is essential to note that current fabrication limitations likely impede achieving such high-performance metamirrors. Future advancements in manufacturing precision are necessary to realize metamirrors capable of reflecting 99.997% of light, not only theoretically but also practically, and to achieve a finesse surpassing 100,000, as per equation (4). The implications of reaching such high finesse values could be significant, potentially opening new avenues in photonic applications and research in high-precision optical metrology.

4 Electric field distribution within the metaatoms

To gain a deeper understanding of the physics underlying the highly reflective metaatoms developed in the previous section, we now shift our focus to an in-depth analysis of individual metaatoms. Considering the dimensions of the metamirrors and the period of their respective metaatoms, we can determine that the metamirror designed for a wavelength of 1064 nm comprises 2703 $\times$ 2703 metaatoms, while the one for 1550 nm consists of 1680 $\times$ 1680 metaatoms. Across the diagonal of each metamirror (from the center to the edge, leveraging symmetry), we select a linearly spaced sample of nine metaatom designs. These designs are presented side-by-side in Figure 8, facilitating initial observations of their topology. Firstly, the metaatoms for 1064 nm exhibit more pronounced variations than those for 1550 nm, as corroborated by Figure 6. Secondly, it is observed that the metaatoms for 1064 nm transition from square shapes at the center to cross-like shapes towards the edge of the metamirror, whereas the reverse trend is observed for 1550 nm. Furthermore, we select three distinctive metaatom designs for each wavelength for simulation in *COMSOL Multiphysics* [43]. The aim is to obtain detailed electric field distributions. These electric field distributions for all three spatial planes are depicted in Figure 8, positioned beneath their corresponding metaatom visualizations. The observed mode shapes appear relatively simplistic and thus more robust. This can be attributed to the low height of the structures, which impedes the development of higher-order modes. It is noted that the majority of the light fields are concentrated within the metaatom structures. Nevertheless, the fields are not entirely confined to these structures; significant field excitations are also

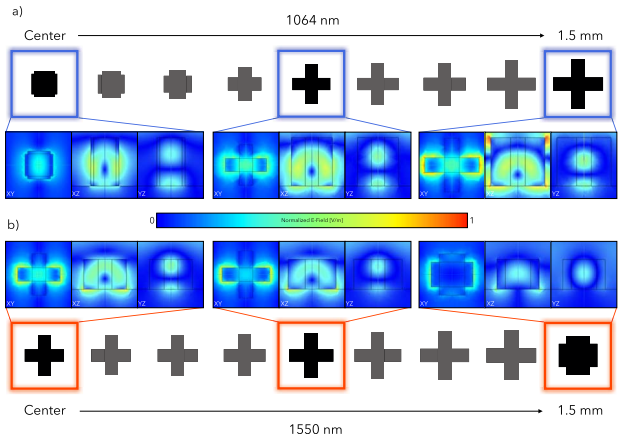

Fig. 8. Electric field distributions of a selection of metaatoms simulated with COMSOL Multiphysics. For both metamirror designs of Figure 7, we visualized 9 linearly spaced metaatoms along the diagonal from the center to the edge of the metamirror, i.e. at 1.5 mm distance. For three, the electric field distributions for all three spacial planes are shown for both (a) 1064 nm and (b) 1550 nm. The field distributions have been normalized across all 18 plots.

observed at the interfaces with the substrate (Silica) and the superstrate (air). In practical experiments, this could result in scattering due to side-wall roughness, potentially diminishing the efficiency of each metaatom. Despite these observations, it is evident that the straight-forward topology of the metaatoms is conducive to the generation of highly reflective optical modes within the structures. The developed framework is inherently adaptable, allowing for future enhancements to include additional elements such as fabrication tolerances and noise contributions [6], thus broadening its applicability and robustness.

5 Conclusion

In this work, we showcased a novel concept of a compact, bispectral optical cavity utilizing twin pairs of low-noise metamirrors. We began by optimizing fixed structural parameters for both metamirrors, disregarding their phase profiles. Subsequent simulations enabled us to identify ideal parameter combinations for flat-phase metamirrors, boasting theoretical reflectivities of 99.9999% at 1064 nm and 99.9995% at 1550 nm. We could then utilize a pathfinding algorithm to render two focusing metamirrors with focal lengths of 6 m and theoretical mean reflectivities of 99.95% at 1064 nm and 99.96% at 1550 nm. Finally, we had an in-depth analysis of the electric fields of a selection of metaatoms, aiming to help understand the underlying physics. Despite its simplicity, our methodology can be readily adapted for multi-wavelength scenarios, offering a versatile platform for creating low-noise, portable optical cavities across various wavelengths.

Acknowledgments

L.S.N. would like to extend his heartfelt thanks to his friends from the "St. Juergens am Strande" club for their support and encouragement.

Funding

The authors gratefully acknowledge the support by the Deutsche Forschungsgemeinschaft (DFG, German Research Foundation) under Germany's Excellence Strategy – EXC-2123 QuantumFrontiers – 390837967. J.D. and S.K also acknowledge partial support by European Association of National Metrology Institutes. This project (20FUN08 NEXTLASERS) has received funding from the EMPIR programme co-financed by the Participating States and from the European Union's Horizon 2020 research and innovation programme.

Conflict of interest

The authors declare no conflicts of interest related to the research presented in this paper. While some of the authors are affiliated with *CAVITY technologies*, there is no direct connection or financial arrangement between the startup and the research conducted at *Technical University of Braunschweig* or *Physikalisch-Technische Bundesanstalt* presented in this work. The startup's activities are unrelated to the specific focus of this paper.

Data Availability Statement

Data underlying the results presented in this paper are not publicly available at this time but may be obtained from the authors upon reasonable request.

Author Contribution Statement

All authors made significant contributions to this work.

References

1 Roberts B.M., Delva P., Al-Masoudi A., Amy-Klein A., Bærentsen C., Baynham C.F.A., Benkler E., Bilicki S., Bize S., Bowden W. (2020) *New J. Phys.* **22**, 093010.
2 Delva P., Lodewyck J., Bilicki S., Bookjans E., Vallet G., Le Targat R., Pottie P.E., Guerlin C., Meynadier F., Le Poncin-Lafitte C., et al. (2017) *Phys. Rev. Lett.* **118**, 221102.
3 Abbott B.P. (2009) *Rep. Prog. Phys.* **72**, 076901.
4 Weiss R. (2018) *Rev. Mod. Phys.* **90**, 040501.
5 Matei D.G., Legero T., Häfner S., Grebing C., Weyrich R., Zhang W., Sonderhouse L., Robinson J.M., Ye J., Riehle F., et al. (2017) *Phys. Rev. Lett.* **118**, 263202.
6 Kroker S., Dickmann J., Rojas Hurtado C.B., Heinert D., Nawrodt R., Levin Y., Vyatchanin S.P. (2017) *Phys. Rev. D* **96**, 022002.
7 Dickmann J., Kroker S. (2018) *Phys. Rev. D* **98**, 082003.
8 Dickmann J., Hurtado C.R., Nawrodt R., Kroker S. (2018) *Phys. Lett. A* **382**, 2275.
9 Dickmann J., Sauer S., Meyer J., Gaedtke M., Siefke T., Bruckner U., Plentz J., Kroker S. (2023) *Commun. Phys.* **6**, 16.
10 Kroker S., Kasebier T., Kley E.B., Tünnermann A. (2013) *Opt. Lett.* **38**, 3336.
11 Shelling Neto L., Dickmann J., Kroker S. (2022) *Opt. Express* **30**, 986.
12 Boyd J.A., Lahaye T. (2024) *Am. J. Phys.* **92**, 50.
13 Kessler S., Hagemann C., Grebing C., Legero T., Sterr S., Riehle F., Martin M.J., Chen L., Ye J. (2012) *Nature Photon.* **6**, 687.
14 Levin Y. (1998) *Phys. Rev. D* **57**, 659–663.
15 Kruk S., Kivshar Y. (2017) *ACS Photon.* **4**, 2638.
16 Balli F., Sultan M., Lami S.K., Hastings J.T. (2020) *Nature Commun.* **11**, 3892.
17 Shi X., Liang Z., Hou E., Yang F., Dong Y., Xin W., Dai R., Jia Y., Xu H. (2023) *Opt. Express* **31**, 41105.
18 Zheng X., Lin J., Wang Z., Zhou H., He Q., Zhou L. (2023) *PhotoniX* **4**, 3.
19 Richards C.A., Ocier C.R., Xie D., Gao H., Robertson T., Goddard L. L., Christiansen R.E., Cahill D.G., Braun P.V. (2023) *Nature Commun.* **14**, 3119.
20 Barbiero M., Calonico D., Levi F., Tarallo M.G. (2022) *IEEE Trans. Instrum. Measure.* **71**, 1.

21 Dawel F., Wilzewski A., Herbers S., Pelzer L., Kramer J., Hild M.B., Dietze K., Krinner L., Spethmann N.C.H., Schmidt P.O. (2023) 2311.11610.
22 Grotti J., Koller S., Vogt S., Häfner S., Sterr U., Lisdat C., Denker H., Voigt C., Timmen L., Rolland A., et al. (2018) *Nat. Phys.* **14**, 437.
23 Hill I.R., Hobson R., Bowden W., Bridge E.M., Donnellan E.A. Curtis, Gill P. (2016) *J Phys. Conf. Ser.* **723**, 012019.
24 Takamoto M., Ushijima I., Ohmae N., Yahagi T., Kokado K., Shinkai H., Katori H. (2020) *Nat. Photon.* **14**, 411.
25 Gellesch M., Jones J., Barron R., Singh A., Sun Q., Bongs K., Singh Y. (2020) *Adv. Opt. Technol.* **9**, 313.
26 Zhao W., Wu H., Fu Y., Ge J., Yang H., Zhang S. (2023) *Front. Phys.* **10**.
27 Davila-Rodriguez J., Baynes F.N., Ludlow A.D., Fortier T.M., Leopardi H., Diddams S.A., Quinlan F. (2017) *Opt. Lett.* **42**, 1277.
28 McLemore C.A., Jin N., Kelleher M.L., Hendrie J.P., Mason D., Luo Y., Lee D., Rakich P., Diddams S.A., Quinlan F. (2022) *Phys. Rev. Appl.* **18**, 054054.
29 Kelleher M.L., McLemore C.A., Lee D., Davila-Rodriguez J., Diddams S.A., Quinlan F. (2023) *Opt. Express* **31**, 11954.
30 Milani G., Rauf B., Barbieri P., Bregolin F., Pizzocaro M., Thoumany P., Levi F., Calonico D. (2017) *Opt. Lett.* **42**, 1970.
31 Leopold T., Schmöger L., Feuchtenbeiner S., Grebin C., Miche P., Scharnhorst N., Leroux I., Crespo Lopez-Urrutia J., Schmidt P. (2016) *Appl. Phys. B* **122**.
32 Cacciapuoti L., Salomon C. (2009) *The European Physical Journal Special Topics* **172**, 57.
33 Kuschewski F., Wüst J., Oswald M., Blomberg T., Gohlke M., Bischof J., Boac A., Alam T., Bußmeier A., Abich K., et al. (2023) *GPS Solu.* **28**, 10.
34 Świerad D., Häfner S., Vogt S., Venon B., Holleville D., Bize S., Kulosa A., Bode S., Singh Y., Bongs K., et al. (2016) *Scientific Rep.* **6**, 33973.
35 Bruzewicz C.D., Chiaverini J., McConnell R., Sage J.M. (2019) *Appl. Phys. Rev.* **6**, 021314.
36 E.S. Team (2020), *Einstein gravitational wave Telescope conceptual design study*, https://doi.org/10.5281/zenodo. 3911261.
37 Jin W., Li W., Orenstein M., Fan S. (2020) *ACS Photon.* **7**, 2350.
38 Steiner S., Kroker S., Käsebier T., Kley E.B., Tünnermann A. (2012) *Opt. Express* **20**, 22555.
39 An S., Zheng B., Shalaginov M.Y., Tang H., Li H., Zhou L., Dong Y., Haerinia M., Agarwal A.M., Rivero-Baleine C., et al. (2022) *Adv. Opt. Mater.* **10**.
40 Johnson S.G., Bienstman P., Skorobogatiy M.A., Ibanescu M., Lidorikis E., Joannopoulos J.D. (2002) *Phys. Rev. E* **66**, 066608.
41 van der Walt S., Schönberger J.L., Nunez-Iglesias J., Boulogne F., Warner J.D., Yager N., Gouillart E., Yu T. (2014) the Scikit-image contributors, *PeerJ* **2**, e453.
42 Ismail N., Kores C.C., Geskus D., Pollnau M. (2016) *Opt. Express* **24**, 16366.
43 COMSOL AB (2023) *COMSOL Multiphysics® v. 5.4*, www. comsol.com.